International Journal of Rock Mechanics & Mining Sciences 192 (2025) 106148

Contents lists available at ScienceDirect

International Journal of Rock Mechanics and Mining Sciences

journal homepage: www.elsevier.com/locate/ijrmms

Effect of Fe-Ni metals on ablation, cavity formation, and recrystallization in laser processing of chondrite meteorite

Yiwei Liu [a], Yanlong Zheng [b], Yi Hu [c,*], Shimin Liu [d], Haizeng Pan [e], Xuhai Tang [a,f,**]

[a] School of Civil Engineering, Wuhan University, Wuhan, 430072, Hubei, China
[b] School of Civil Engineering, Southeast University, Nanjing, 211189, China
[c] The Institute of Technological Sciences, Wuhan University, Wuhan, 430072, Hubei, China
[d] Department of Energy and Mineral Engineering, G3 Center and EMS Energy Institute, The Pennsylvania State University, University Park, PA, 16802, USA
[e] Institute of Rock and Soil Mechanics, Chinese Academy of Sciences, Wuhan, 430071, China
[f] Wuhan University Shenzhen Research Institute, Shenzhen, 518057, China

ARTICLE INFO

Keywords:
Space mining
Laser
Fe-Ni metals
Asteroid meteorites
Planetary rock mechanics

ABSTRACT

Laser processing is an effective method for cutting extraterrestrial rocks, making it potentially useful for space mining. By comparing laser processing of terrestrial basalt and the Hammadah al Hamra 346 (HaH 346) chondrite meteorite, we investigated the influence of iron-nickel (Fe-Ni) metals on laser-induced melting, cavity formation, and recrystallization. Experimental results revealed that the presence of Fe-Ni metals significantly reduces the depth of laser-induced cavities in HaH 346 meteorite while increasing their width, as the melting metal strongly absorbs laser energy. X-ray computed tomography results demonstrated that the laser-induced cavities in the HaH 346 meteorite are much shallower than those in basalt. Microstructural analysis indicated that Fe-Ni metals in HaH 346 recrystallize into ellipsoidal crystal formations, while silicates form complex and nest-like structures. Furthermore, the temperature of Fe-Ni metal during laser irradiation is significantly lower than that of silicate and mixed zones. Due to the vacuum environment of space, Fe-Ni metals are widely present in planetary rocks. Our study highlights the potential of laser cutting for future space mining and the key differences between laser cutting on Earth and in space.

1. Introduction

Laser drilling, cutting, ablation, and processing of planetary rocks has attracted widespread interest due to their potential applications in space mining and space construction.[1–6] Laser processing is particularly advantageous in space mining because it involves no moving parts, which produces minimal counter-torques and is crucial for maintaining stability on low-gravity bodies.[7] It can be applied to process a wide range of materials, from dust to metal. Due to its non-contact nature, laser processing can be operated remotely without direct surface contact, which minimizes the need for landing. This enhances efficiency, flexibility, and safety while reducing resource consumption. Compared to traditional mechanical drills, lasers offer greater precision and highly focused energy, enabling targeted drilling and ablation. In extraterrestrial construction, lasers are versatile tools. Laser ablation is able to vaporize or sublimate the surface of asteroids or lunar regolith, selectively removing material and exposing valuable resources, such as iron, nickel, cobalt, and platinum group metals.[8–10] This supports in-situ resource utilization (ISRU) for long-term space exploration and resource demands. By sintering meteoritic or regolith materials, lasers can be used to create structural components.[3,11–14] Additionally, lasers can extract volatiles from planetary bodies such as the Moon or Mars, where water ice or other substances (e.g., CO_2, ammonia) may be trapped in the regolith. Heating these materials with lasers can release trapped gases or liquids, which is useful for obtaining water or other volatiles for life support or fuel.[15]

The effects of laser processing on rock-forming minerals in extraterrestrial geomaterials have been investigated by some researchers. Anthony et al. studied the effects of laser irradiation on olivine, pyroxene and serpentine, which are minerals commonly found on asteroids, and discussed how different laser pulse parameters influence hole depth and removal volume.[7,16] Matsuoka et al. conducted pulsed laser

* Corresponding author.
** Corresponding author. School of Civil Engineering, Wuhan University, Wuhan, 430072, Hubei, China.
E-mail addresses: huxiaoyi@whu.edu.cn (Y. Hu), xuhaitang@whu.edu.cn (X. Tang).

https://doi.org/10.1016/j.ijrmms.2025.106148
Received 21 October 2024; Received in revised form 30 April 2025; Accepted 3 May 2025
Available online 20 May 2025
1365-1609/© 2025 Elsevier Ltd. All rights are reserved, including those for text and data mining, AI training, and similar technologies.

irradiation experiments to simulate micrometeorite impacts on C-type asteroids, investigating changes in reflection spectra, mineralogy, and chemical composition.[17] Hamann et al. examined the melting and evaporation of sandstone, iron meteorites, and basalt under continuous-wave laser irradiation, analyzing the results using high-speed imaging, temperature measurements, and petrological analysis.[18] However, laser-asteroid rock interactions remain insufficiently explored. Previous research has largely overlooked Fe-Ni metal minerals in meteorites. As common constituents of asteroid material and components that differ significantly from Earth rocks, the behavior of Fe-Ni minerals under laser irradiation remains poorly understood. These Fe-Ni metal minerals have distinctive thermal, chemical, and physical properties that may significantly affect the macroscale mechanical properties of the asteroid rock.

This study investigates the effects of laser irradiation on Fe-Ni metals in the Hammadah al Hamra 346 (HaH 346) asteroid meteorite. Earth basalt, which is primarily composed of silicate, was used as a reference material. We employed electron microscopes, X-ray computed tomography (XCT), and temperature monitoring to analyze the effects of Fe-Ni metals on the surface morphology, geometry of laser-induced cavities, temperature evolution, and recrystallization during cooling. These findings contribute to a better understanding of laser interactions with asteroid surfaces.

2. Experimental setups

2.1. Samples

The experiment utilized the Hammadah al Hamra 346 (HaH 346) chondrite meteorite, which fell on August 26, 2018, in the southern region of Jabal al Gharbi, Libya. The original meteorite features a matte black and fresh fusion crust without significant wind abrasion. The interior appears light gray, with some areas showing slight brown staining from exposed metal (see Fig. 1(a)). The meteorite is classified as an L6 ordinary chondrite, primarily composed of olivine and low-calcium pyroxene, with a matrix that includes plagioclase, Fe-Ni metal (kamacite and taenite), troilite, merrillite, and trace amounts of unclassified minerals. Tang et al. provided detailed mineralogical and micromechanical characterizations of this meteorite.[19] The mineral proportions in the meteorite are given in Table 1. Based on analysis using the TESCAN Integrated Mineral Analyzer and optical microscopy, the main rock-forming minerals in the HaH 346 meteorite were determined to be 42.3 % olivine, 33.2 % low-calcium pyroxene, 12.5 % feldspar, 5 % Fe–Ni metal, 5 % troilite, 1.2 % merrillite, and 0.8 % unidentified minerals. A cubic bulk sample was cut from the interior of the meteorite (see Fig. 1(b)).

Table 1
Mineralogical information of HaH 346 asteroid meteorites and the basalt sample.

Mineral	Density (kg/m^3)	Proportions in samples	
		HaH 346	Basalt
Olivine	3410	42.3	13.0
Pyroxene	3272	33.2	22.0
Plagioclase	2580	12.5	65.0
Fe-Ni metal	7900–8010	5.0	/
Troilite	4610	5.0	/
Merrillite	3100	1.2	/

Basalt is a common volcanic rock and a primary component of Earth's oceanic crust. It is also widespread on the Moon, Mars, and other celestial bodies. In terms of mineral composition, basalt is the Earth rock most analogous to exoplanetary rocks, containing minerals such as olivine, pyroxene, plagioclase, and ilmenite. However, extraterrestrial rocks often contain unique rock-forming minerals, such as Fe-Ni metals and troilite. In this study, basalt was used as a comparative reference. The basalt sample was obtained from Hainan, China, as shown in Fig. 1 (c). It is composed of 13 % olivine, 22 % pyroxene, and 65 % plagioclase. The densities and proportions of the minerals in both the HaH 346 meteorite and the basalt sample are presented in Table 1. The density data were determined based on existing literature and the WebMineral database (https://webmineral.com).[20,21]

2.2. The laser system and laser irradiation experiments

The laser-induced melting and drilling experiments were conducted using a self-developed laser test system at Wuhan University. The system consists of four components: a laser, a cooler, a welding gun, and a helium cylinder, as shown in Fig. 2. A three-axis moving frame was designed to control the movement of the laser gun. The system is equipped with a Nd: YAG laser operating in the infrared spectrum at a wavelength of 1064 nm. It is a continuous-wave laser capable of

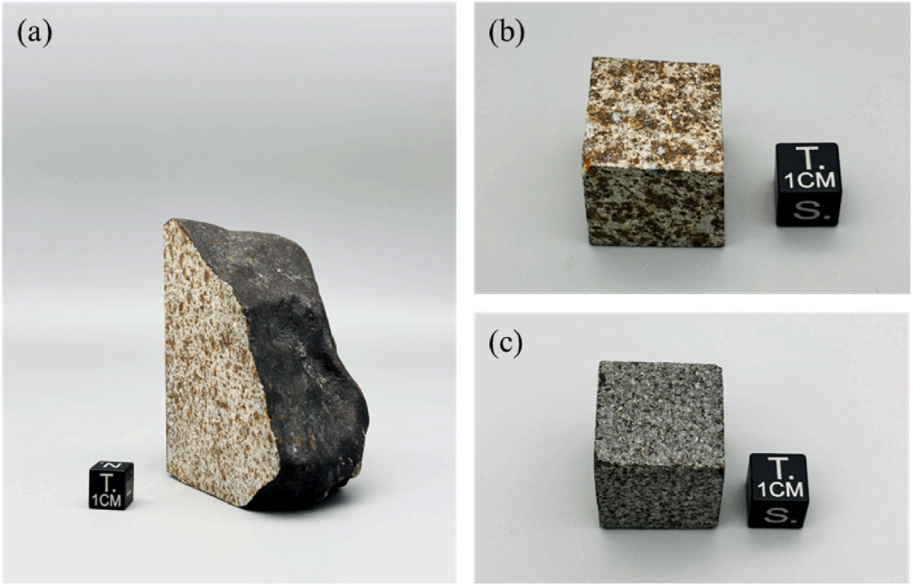


Fig. 1. HaH 346 asteroid meteorites and the basalt specimen. (a) The original meteorite, showing a matte black and fresh fusion crust. (b) HaH 346 meteorite sample. (c) The basalt sample.

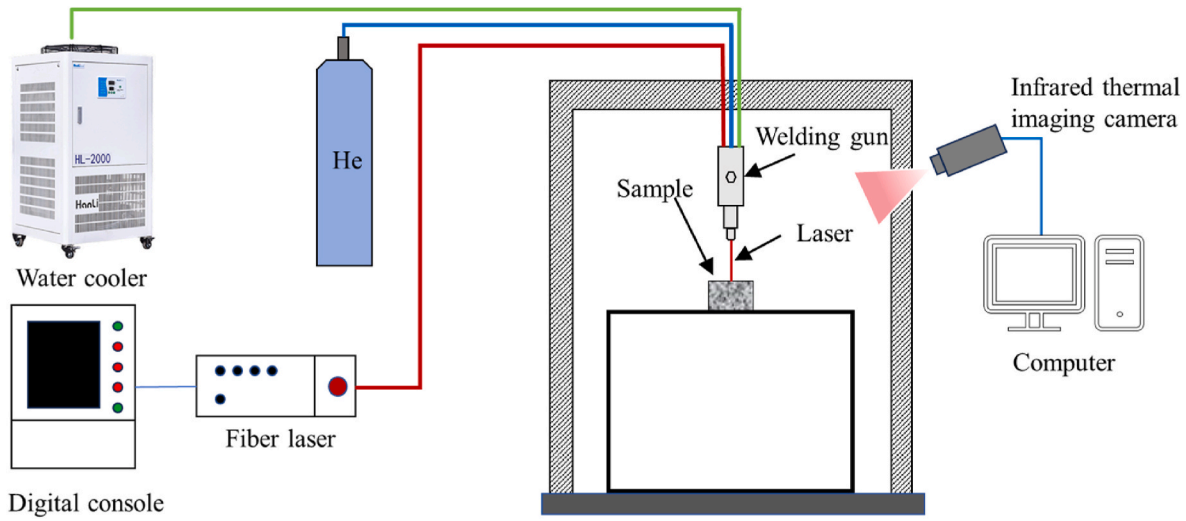


Fig. 2. The laser system used in the experiments.

sustained operation at maximum power, with a maximum output of 2 kW and a focal spot size of 1 mm. In the experiment, the samples were placed on cylindrical rock bases. The irradiation power used was 500 W, and the duration of laser irradiation for all samples was 15 s. To eliminate the influence of varying focal positions (which affect spot size), the working distance was consistently maintained at 10 cm.

Fe-Ni metal is a distinctive feature of meteorites and is absent in terrestrial rocks due to the rapid oxidation and rusting of iron in Earth's oxygen- and water-rich environment. Based on the mineral distribution, the surface of the meteorite was categorized into three zones according to Fe-Ni metal content: (1) silicate zone, consisting of pyroxene and olivine spherules; (2) mixture zone, composed of Fe-Ni metal flakes and fine-grained silicates; (3) Fe-Ni metal zone, entirely composed of Fe-Ni metal grains. To study the effect of Fe-Ni metal on laser-induced melting in the HaH 346 meteorite, four laser irradiation experiments were conducted: on the silicate zone (case 1), the mixture zone (cases 2 and 3), and the Fe-Ni metal zone (case 4). In case 1, the laser targeted a large spheroidal silicate mineral with 0 % Fe–Ni metal content. In cases 2 and 3, the laser was focused on the mixture zone; case 2 had slightly less Fe-Ni metal content than case 3. In case 4, a Fe-Ni metal piece approximately 4 mm in diameter was selected, with 100 % Fe–Ni metal content. The basalt samples were irradiated under the same laser parameters.

2.3. Temperature monitoring

A FLIR 600 infrared microbolometer was used for spatially and time-resolved temperature measurements. The device features a 640 × 480 pixels detector capable of sensing temperature differences as small as 50 mK. Image transfer in window mode at 50 Hz was used for high-speed data capture. The device measures temperatures ranging from 100 to 2100 °C with an accuracy of ±2 °C. The focus of the imaging process was on recording surface temperature changes. Thus, internal temperatures could not be measured. Infrared image analysis provided data on the heating rate and surface temperature distribution of the samples.

2.4. Morphology and structural characterization

The electron microscope AO-HK830 was used to observe the samples and characterize surface morphology after laser irradiation. X-ray computed tomography (XCT) was utilized to analyze the internal structure and pore formation of the meteorite post-irradiation. To examine the laser-induced thermal zones, the HaH 346 meteorite sample was cut along the melt track, parallel to the laser beam trajectory, using a metallographic sample cutting machine. A scanning electron microscope (SEM) was then employed to image the meteorite cross-section and characterize the molten zones following laser irradiation. All images were taken from the original cut surface without additional polishing to avoid rapid oxidation of iron-bearing minerals, which can be introduced during the polishing process.

3. Observation of meteorites before laser irradiation

HaH 346 is an ordinary chondrite, primarily composed of silicate minerals and Fe-Ni metals, and is classified as an L6 lithological type. The "L" denotes "low metal", while the "6" refers to the petrographic type, indicating the degree of thermal metamorphism the meteorite has undergone. L6 chondrites have experienced significant thermal metamorphism, resulting in the development of a fine-grained matrix and the recrystallization of minerals, which gives the meteorite a more homogenized texture compared to less metamorphosed types. This metamorphism also imparts a light gray color to the HaH 346 meteorite. Additionally, chondrules—spherical grains typical in chondritic meteorites—are less distinct in number in L6 chondrites due to thermal metamorphism effects.

Fig. 3 shows electron microscope images of the HaH 346 meteorite surface. Fe-Ni metal and troilite are uniformly distributed throughout the stone. They appear as small, silver-colored flakes dispersed within the meteorite's matrix, with the largest grains measuring between 1 mm and 4 mm in length, as shown in Fig. 3(a). Bronze-colored troilite is scattered among the fine-grained matrix. Limonitic staining around Fe-Ni metal and troilite indicates slight weathering due to exposure to oxygen and moisture. No visible oxidation was observed in the silicate minerals. Despite extensive metamorphism, some chondritic structures remain in the meteorite, as shown in Fig. 3(b) and (c). These include gray pyroxene spherules and light green olivine spherules, with pyroxene spherules measuring 3–5 mm in diameter and olivine spherules approximately 2–3 mm. Fig. 3(d) illustrates the three zones in HaH 346, categorized by Fe-Ni metal content.

4. Effect of Fe-Ni metal on melting and cavity formation by laser irradiation

4.1. Comparison of laser-induced cavities in HaH 346 meteorite and basalt

Fig. 4 presents XCT images of the laser-induced cavities in the silicate zone of HaH 346 asteroid meteorite (Fig. 4(a)) and in the basalt (Fig. 4

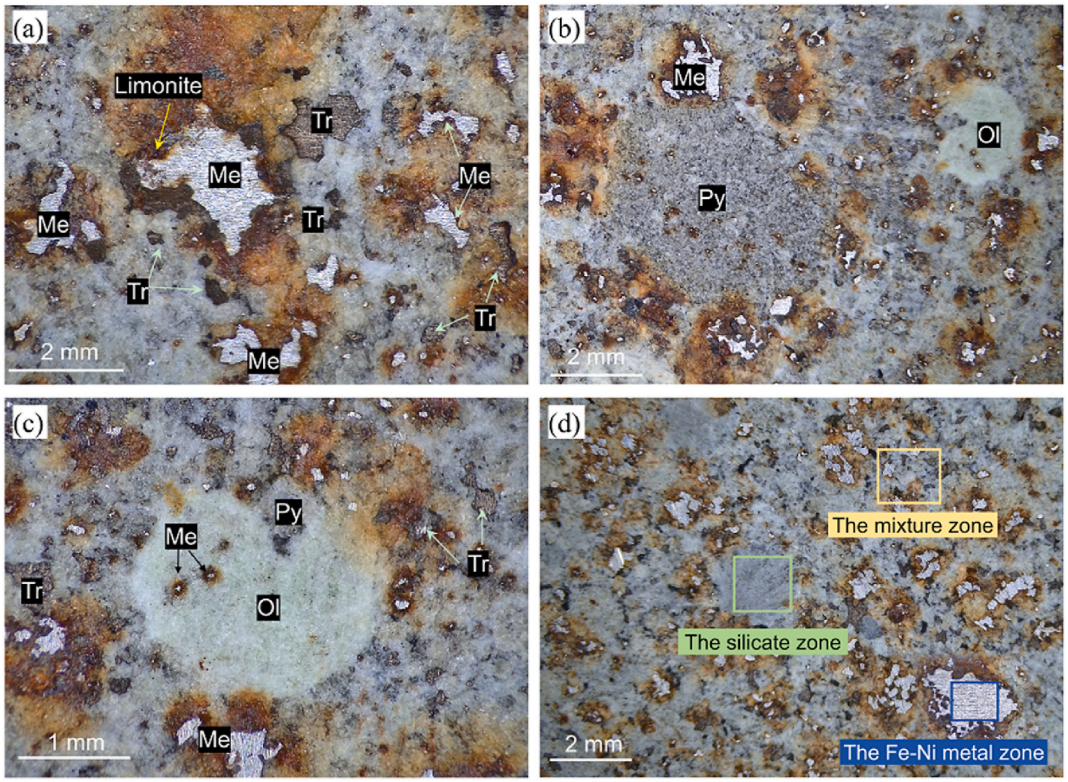


Fig. 3. Microscopy images of the HaH 346 meteorite. Me: Fe-Ni metal; Tr: troilite; Py: pyroxene; Ol: olivine. (a) Fe-Ni metals distributed across the surface, with limonitic staining indicating slight weathering; (b) Chondrules primarily composed of large silicate grains (pyroxene and olivine); (c) Magnified image of an olivine grain; (d) The HaH 346 surface is categorized into three zones based on Fe-Ni metal content: the silicate zone, the mixture zone and the Fe-Ni metal zone.

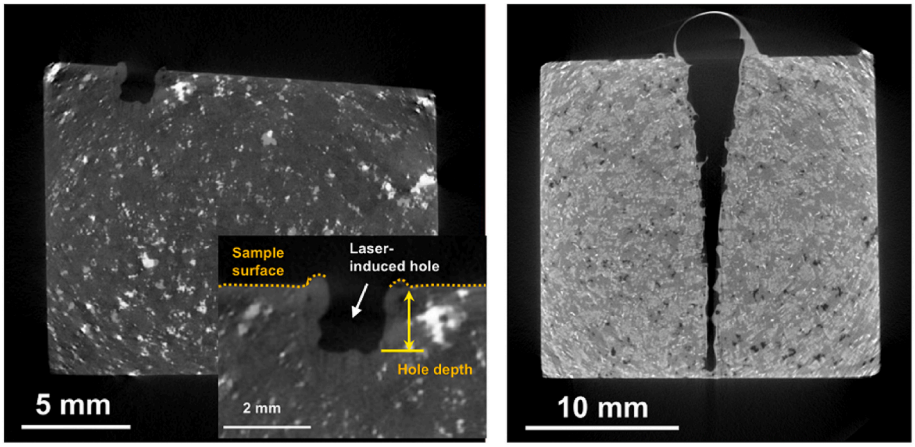


Fig. 4. XCT images of (a) the HaH 346 asteroid meteorite and (b) basalt.

(b)). These images show cross-sections of the cavities in the direction parallel to the laser beam trajectory. The cavity in the silicate zone of the HaH 346 meteorite is significantly shallower and differs in shape compared to the cavity in basalt. As shown in the magnified view in Fig. 4(a), the meteorite cavity is shallow, with vesicles formed by partial melting visible around it. The cavity bottom is flat, and the laser-induced material removal did not penetrate deeply. In contrast, laser irradiation formed a much deeper cavity in basalt, nearly penetrating the entire sample, as shown in Fig. 4(b). The basalt cavity is spindle-shaped, with a progressively narrower diameter at greater depths.

Fig. 5 shows the reflected light color from laser irradiation, which varies between the meteorite and basalt. Reflected light from Fe-Ni metal appears purple, while light reflected from silicate minerals in both the meteorite and basalt appears bright warm white. In the mixture zone, the reflected light is a blend of purple and warm white. The purple hue results from the excitation of electrons on the metal surface, which generates a plasma glow. This plasma refracts and absorbs the incident laser, creating a shielding effect that reduces laser energy coupling with the meteorite and influences melt depth. Increased plasma accumulation can cause greater dispersion of laser energy, reducing surface temperature and melt depth.

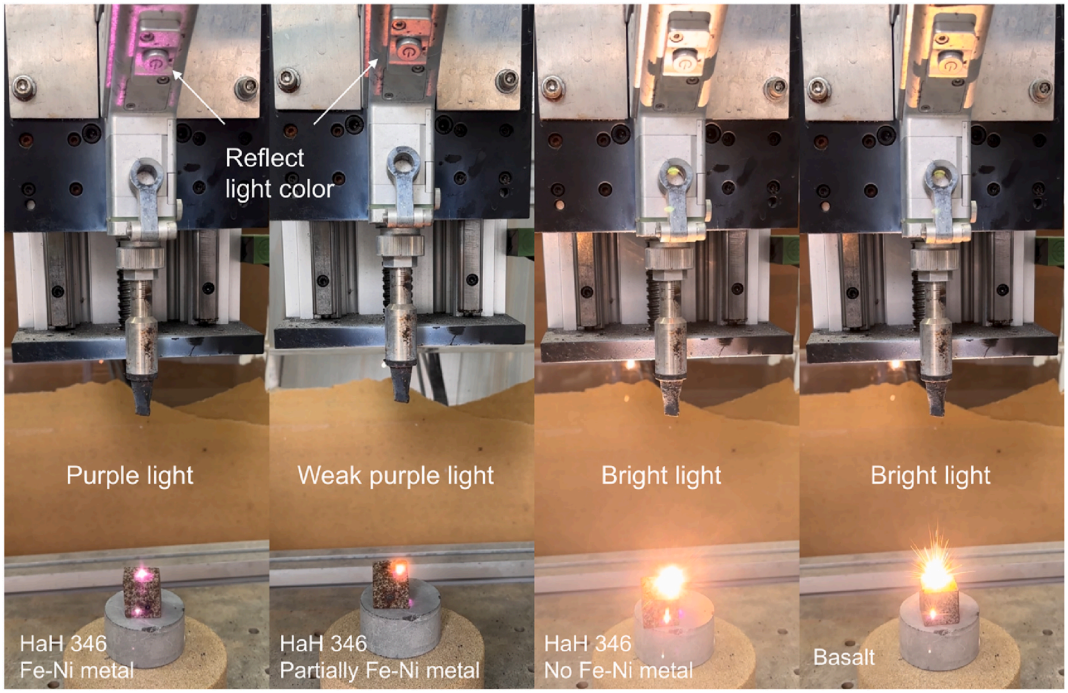


Fig. 5. Reflected light from laser irradiation on the meteorite and basalt.

4.2. Effect of Fe-Ni metal content on the morphology of laser-induced cavities

Four laser irradiation experiments were conducted on the HaH 346 asteroid meteorite. Surface damage from the laser is detailed in Table 2, along with the morphology of the resulting cavities caused by mineral melting and vaporization. From case 1 to case 4, the Fe-Ni metal content increased progressively from 0 % to 100 %. Microscopy was used to observe surface melting states and cavity formation, while XCT was employed to analyze the internal cavity structure along the depth direction. Microscopic images showed that the heat-damaged zones on the meteorite surface were roughly circular, with accumulated melt material around the cavity edges. The laser irradiation in the silicate zone (case 1) and the mixture zone (case 2 and 3) produced cavities on the meteorite surface, with the cavity depth decreasing from case 1 (deepest) to case 3 (shallowest). In case 1, the cavity contained light green glassy melt, indicating the primary melting of silicate minerals. In case 2, the laser created a nearly hemispherical pit with a thin black metal shell at the bottom. In case 3, the laser induced a wider but shallower cavity with a flat bottom reflecting polyhedral metallic fragments. In case 4, targeting the 100 % Fe–Ni metal zone, the laser caused surface fusion and formed a small central hole. The melt surface was oxidized to black.

XCT images revealed the cross-sectional structure of the melt zones in the HaH 346 meteorite. The deepest and most cylindrical cavity was observed in the silicate zone (case 1), which lacked Fe-Ni metal. In the mixture zones (cases 2 and 3), shallower arc-shaped cavities were formed. Vesicular structures were observed, caused by preferential melting of specific minerals. When the laser was applied to the 100 % Fe–Ni metal zone (case 4), molten Fe-Ni metal overflowed onto the surface and resolidified as a mass above it. This suggests that the laser reached temperatures sufficient to melt but not vaporize the Fe-Ni metal, leaving a solidified mass. This is confirmed in the XCT image shown in Table 2(c), where the resolidified Fe-Ni metal appears darker than the original, indicating a lower density.

Fig. 6 presents the depth, width, and surface area of the melt zones produced by laser irradiation. The cavity depths for the silicate zone (case 1), mixture zones (cases 2 and 3), and Fe-Ni metal zone (case 4) were 2.2 mm, 1.2 mm, 0.3 mm, and 0 mm, respectively. In case 4, the Fe-Ni metal melted and overflowed the surface, resulting in no recessed cavity (hence the recorded depth is zero). The corresponding cavity widths were 2 mm, 3.2 mm, 3 mm, and 5 mm, and the surface areas were 4.9 mm^2, 7.8 mm^2, 7.6 mm^2, and 9.1 mm^2, respectively.

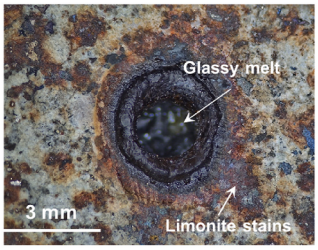
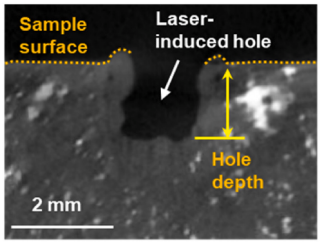
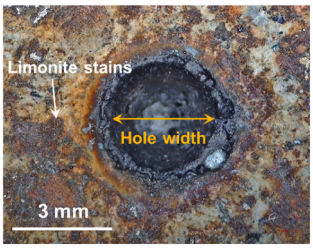
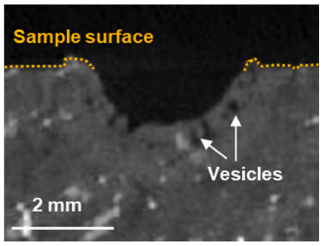
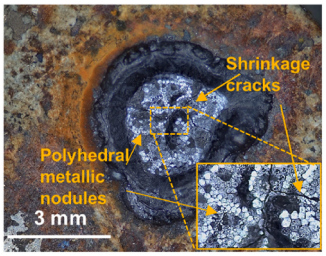
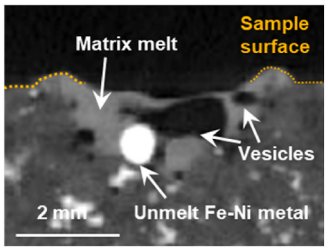
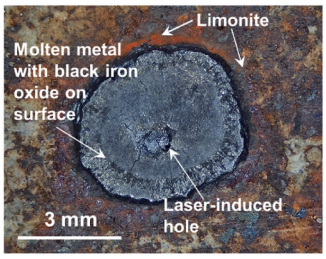
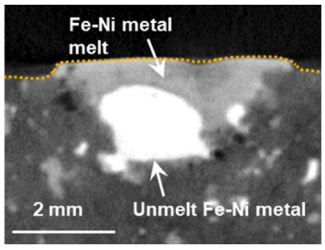
These results indicate that as the Fe-Ni metal content increased, the depth of the laser-induced cavities significantly decreased, while the width and surface area increased. This phenomenon may be attributed to the unique behavior of Fe-Ni metal. When irradiated, Fe-Ni metal rapidly melts and absorbs laser energy, preventing the beam from penetrating deeper. This inhibits the removal of the silicate mineral underneath the metal and leads to shallower cavities. Meanwhile, restricted laser penetration causes lateral energy dispersion along the cavity wall, resulting in broader cavity widths and larger surface areas.

5. Effect of Fe-Ni metal on temperature changes induced by laser irradiation

Infrared thermometers were used to record the temporal and spatial temperature changes on the surface of meteorite during laser irradiation, as shown in Fig. 7(a) and (b). Surface temperatures were captured at a time resolution of 50 Hz, providing detailed spatial temperature distribution data. The highest surface temperature occurred at the laser focal point and decreased radially outward. Fig. 7(c) illustrates the temperature rise curves for basalt and for the silicate, mixture, and Fe-Ni metal zones of the meteorite during laser irradiation.

The maximum recorded temperature in the Fe-Ni metal was 1034.4 °C, which is significantly lower than those in the silicate, mixture, and basalt. The maximum temperatures for silicate and mixture zones in HaH 346 meteorite were 1710.7 °C and 1485.5 °C, respectively, while basalt reached 1656.7 °C. After the laser was turned off, the surface temperatures of the meteorite dropped sharply. Within 1 s after irradiation stopped, the temperatures in the silicate, mixture, and Fe-Ni metal zones decreased by 32.8 %, 28.3 %, and 15.0 %, reaching 1149 °C, 1065.1 °C, and 879.6 °C, respectively. The temperature of the basalt dropped by 50 % within 1 s, from 1656.7 °C to 828.8 °C. More detailed temperature data are provided in Table 3. It should be noted that the infrared thermometer can only measure surface temperatures. The true

Table 2
Mineral melting characteristics and laser-induced cavities in different mineral zones.

	Case	Microscopy image	XCT images
(a) The silicate zone (0 % Fe–Ni)	1		
(b) The mixture zone	2		
	3		
(c) The Fe-Ni metal zone (100 % Fe–Ni)	4		

maximum temperatures may occur inside the laser-induced cavities, making the recorded data potentially lower than the actual peak temperatures.

6. Recrystallization of HaH 346 meteorites during the cooling process

To analyze the recrystallization of laser-induced molten materials in the HaH 346 meteorite, the sample was sectioned along the melt track parallel to the laser beam trajectory. SEM was employed to characterize the post-cooling melting profile. Figs. 8–10 show cross-section images of cavities in the silicate zone, Fe-Ni metal zone, and mixture zone, respectively. The SEM images reveal significant differences in the microstructures of molten silicates, Fe-Ni metals, and their mixtures after laser-induced melting and cooling.

Fig. 8(a) shows the SEM cross-section of the laser-induced cavity in the silicate zone. The crystallization morphology of molten silicate exhibits marble-like patterns (Fig. 8(b), marked as 1). The cavity sides and bottom show severe cracking (Fig. 8(c) and (d), marked as 2 and 3), likely due to volumetric contraction during cooling. The inner surface of the melt presents elongated, plate-like structures approximately 50 μm wide and several hundred micrometers to 1 mm long (Fig. 8(e), marked as 4). These plates interweave to form nest-like structures, each containing numerous pores. Smaller rod-like structures are also present (Fig. 8(f), marked as 5). Spherical vesicles formed by preferential mineral melting are observed on the inner walls of the melt.

Metal particles larger than 3 mm are categorized as metal clumps. Fig. 9(a) presents a cross-sectional view of a Fe-Ni metal clump (~4 mm in size) and its associated melt. The light silver zone represents the original Fe-Ni metal (marked as 2), which has a higher density, while the gray zone represents the molten Fe-Ni metal (marked as 1). The section of original Fe-Ni metal is flat, with a few scratches from the cutting (Fig. 9(b)). The molten section shows a finer internal structure, enlarged in Fig. 9(c) and (d). The crystalline structure displays a complex but orderly pattern with clearly defined boundaries. Ellipsoidal crystals resembling mangosteen segments grow concentrically around a central columnar structure. These crystals stack in an orderly manner and interweave at nearly orthogonal angles, forming a distinctive microscale texture.

Fig. 10(a) shows the cross-sectional image of laser-induced cavity in the mixture zone, which includes Fe-Ni metal, troilite, and silicate minerals. Sulfide metal vesicles are observed within the melt, as shown in Fig. 10(a) and (b).The melting zone in the mixture zone has a conical cross-section with a clear boundary between the melting zone (marked

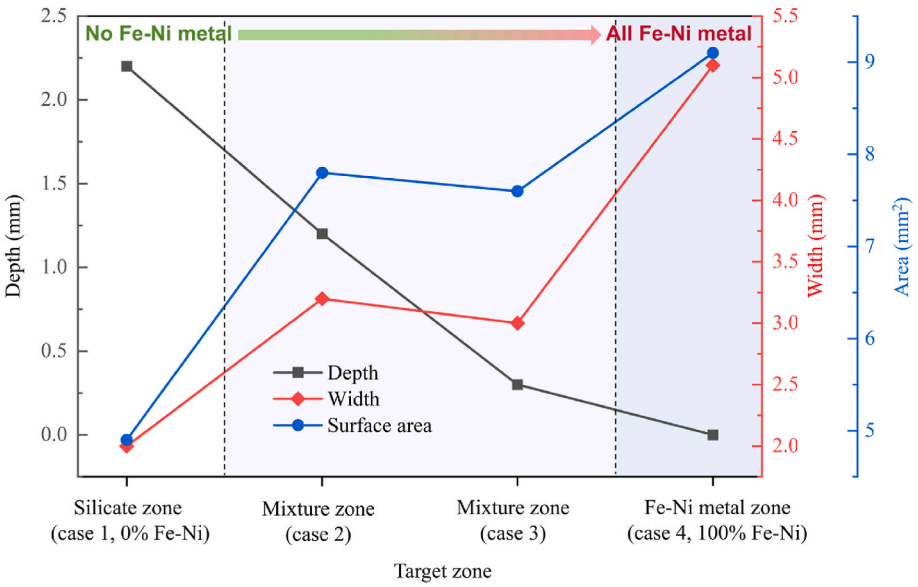


Fig. 6. Effect of Fe-Ni metal content on the depth, width, and surface area of the melt zones produced by laser irradiation in the silicate zone (0 % Fe–Ni), the mixture zone, and the Fe-Ni metal zone (100 % Fe–Ni).

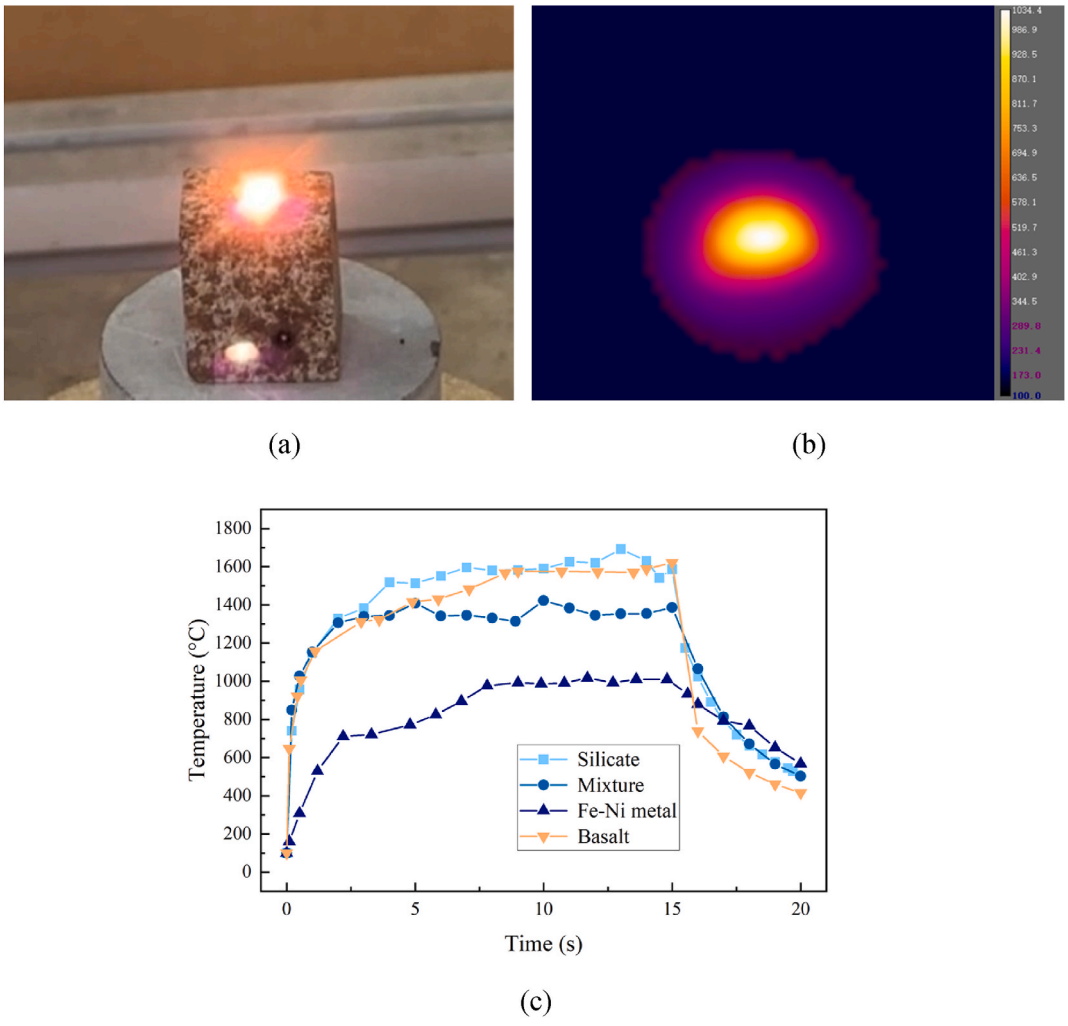


Fig. 7. (a) The HaH 346 meteorite during experiment. (b) Corresponding temperature map of Fig. 7(a) at the time of maximum temperature. (c) Maximum temperature curves during irradiation and for 5 s laser cessation, measured for basalt and the silicate, mixture, and Fe-Ni metal zones in the meteorite.

Table 3
Laser-induced temperature in HaH 346 asteroid meteorites and basalt.

	Maximum Temperature (°C)	Heating rate (°C/s)			Cooling rate (°C/s)		
		1st s	2nd s	3rd s	1st s	2nd s	3rd s
Silicate	1710.7	1150.4	179.0	252.9	561.7	230.5	132.3
Mixture	1485.5	1153.1	153.2	44.6	420.4	251.4	141.4
Fe-Ni metal	1034.4	463.5	222.9	69.3	154.8	85.5	26.3
Basalt	1656.7	1168.9	92.7	65.2	827.9	132.2	84.6

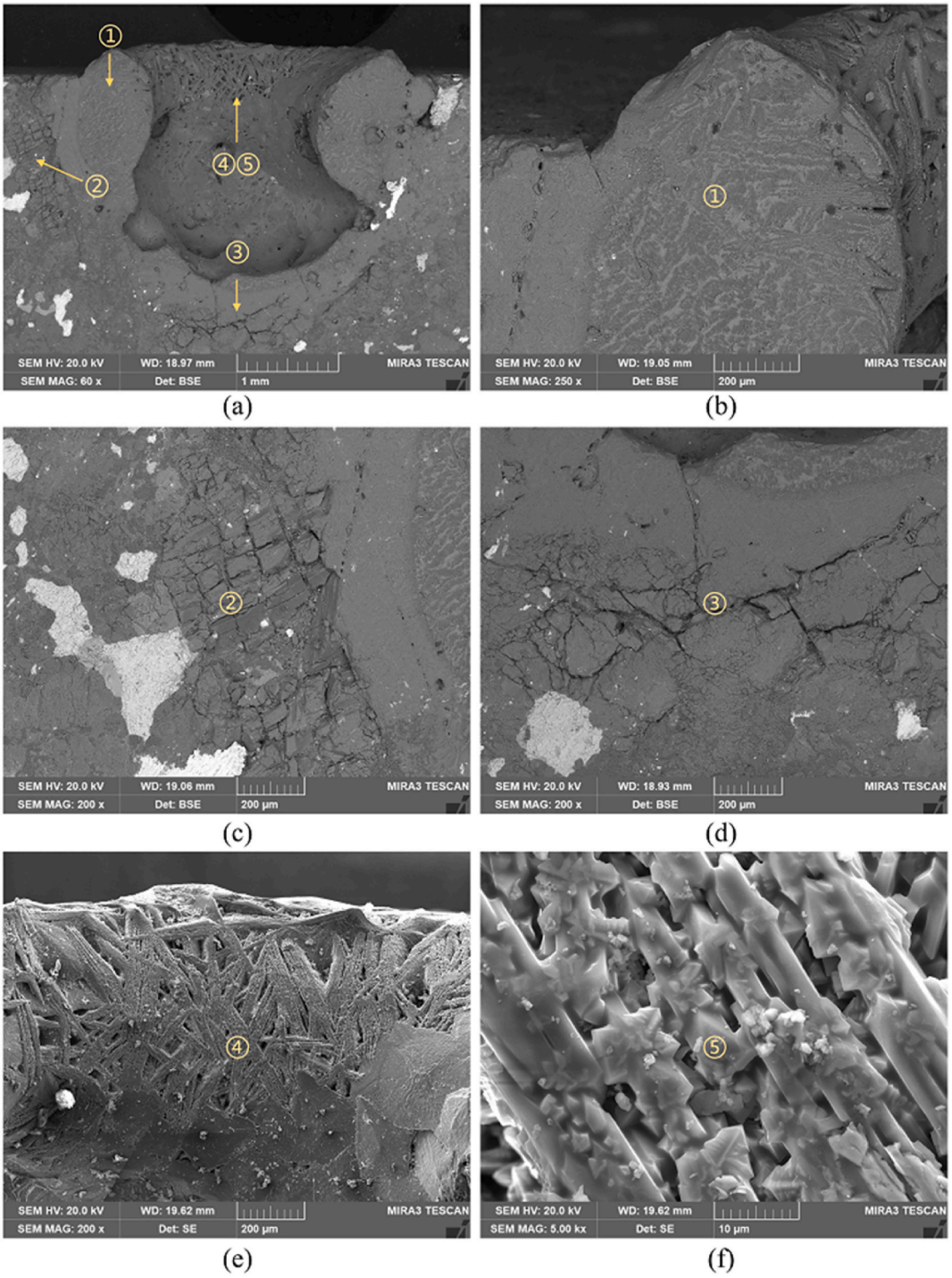


Fig. 8. Recrystallization in the silicate zone of the HaH 346 meteorite after cooling. SEM images captured within the molten silicate chondrule profile. (a) Internal profile of the laser-induced cavity. (b) Marble-like patterns in the cross-section. (c) and (d) are the thermally induced cracks near the cavity. (e) Nest-like structures on the inner surface of the melt. (f) Enlarged view of elongated, plate-like structures.

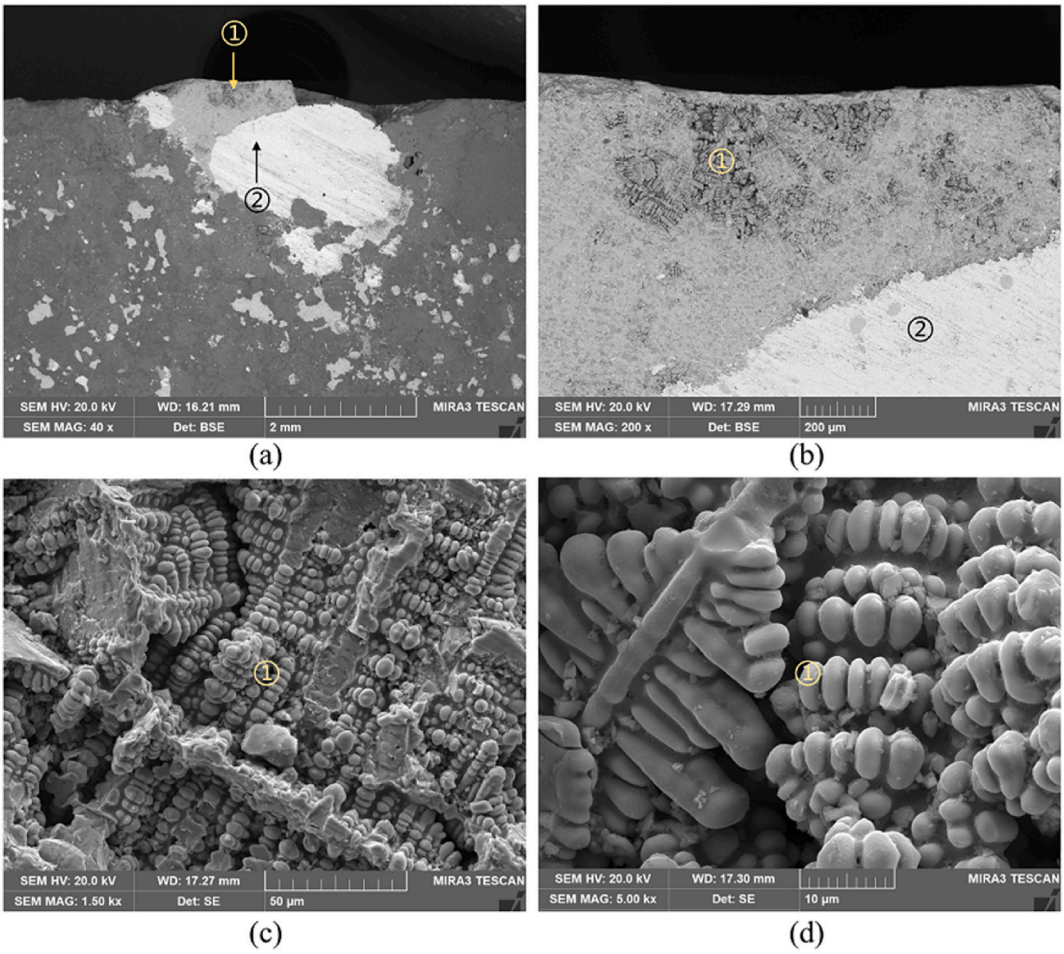


Fig. 9. Recrystallization of Fe-Ni metal in the HaH 346 meteorite after cooling. SEM images captured within the molten Fe-Ni metal profile. (a) Cross-section of the molten Fe-Ni metal. (b) Surface of the original Fe-Ni metal and the molten metal. (c) and (d) are enlarged images of the fine crystalline structures.

as 1) and the transition zone (marked as 2). Elongated and needle-like crystal textures are observed within the melt, as shown in Fig. 10(c). Elongated and needle-like crystal textures are observed within the melt (Fig. 10(c)). These crystals, likely formed by rapid crystallization of the meteorite melt, are approximately 100–300 μm in length and 20–40 μm in width. The elongated metal bands most likely result from the immiscibility of the Fe-Ni metal melt and silicate melt. The high temperature induced by laser irradiation causes complete melting of the meteorite matrix and alters the mineral structures. Fe-Ni metal and silicate minerals melt into immiscible phases, which separate during cooling due to differences in density and melting points, resulting in elongated, needle-like metal crystals embedded in the silicate matrix. In the transition zone, white mineral veins within silicate grains are visible, which are produced by sulfide metal exsolution (Fig. 10(d)). Significant micro-cracking is also observed within the melt, with some cracks extending into the transition zone between the melt and the unaffected area. Such extensive cracking is not observed in the melts of either Fe-Ni metal or silicates alone, likely due to thermal heterogeneity during cooling.

7. Discussion

Laser-rock interactions involve four main removal mechanisms: ablation, melting, spallation, and sputtering. Experimental results show that lasers are less effective on Fe-Ni metals than on silicate minerals. In silicates, all four mechanisms are active: ablation is indicated by smoke emission (Fig. 11(a)), melting by the presence of glassy residues (Table 2 (a)), and spallation and sputtering by the ejection of high-temperature fragments (Fig. 11(b)). The brittleness and low fracture toughness of silicates make them more prone to spallation, while the presence of water molecules in their structure may enhance vaporization and promote sputtering.[22–25] In contrast, Fe-Ni metal is primarily removed through melting. Fig. 11(c) shows the formation of a high-temperature molten pool in the Fe-Ni metal. Due to its high density, reflectivity, and thermal conductivity, Fe-Ni metal absorbs less laser energy and is less efficiently removed, resulting in shallower cavities. Although basalt and meteorites share similar major mineral components, the presence of Fe-Ni metal in meteorites significantly limits laser penetration and material removal.

In this work, we found that the Fe-Ni metal content significantly affects the depth and morphology of laser-induced cavities. These findings offer implications for future mining on S-type (stony) asteroids, which share compositional similarities with HaH 346 meteorites. More broadly, the results are applicable to planetary bodies with oxygen-deficient atmospheres, where planetary rocks commonly contain iron-nickel metal or elemental iron. As a potential auxiliary tool for space mining, lasers will inevitably interact with such planetary rocks. This study provides insights into the interaction between lasers and rock containing iron-nickel or elemental iron, offering predictive value for laser-based operations on exoplanets and other extraterrestrial surfaces.

Several limitations should be noted. The laser experiments were performed under atmospheric conditions, which may affect material responses due to differences in pressure and temperature. Future experiments will be conducted in vacuum chambers to better simulate space environments. Additionally, each planetary body has undergone a long history of thermal evolution.[26,27] During this process, structural

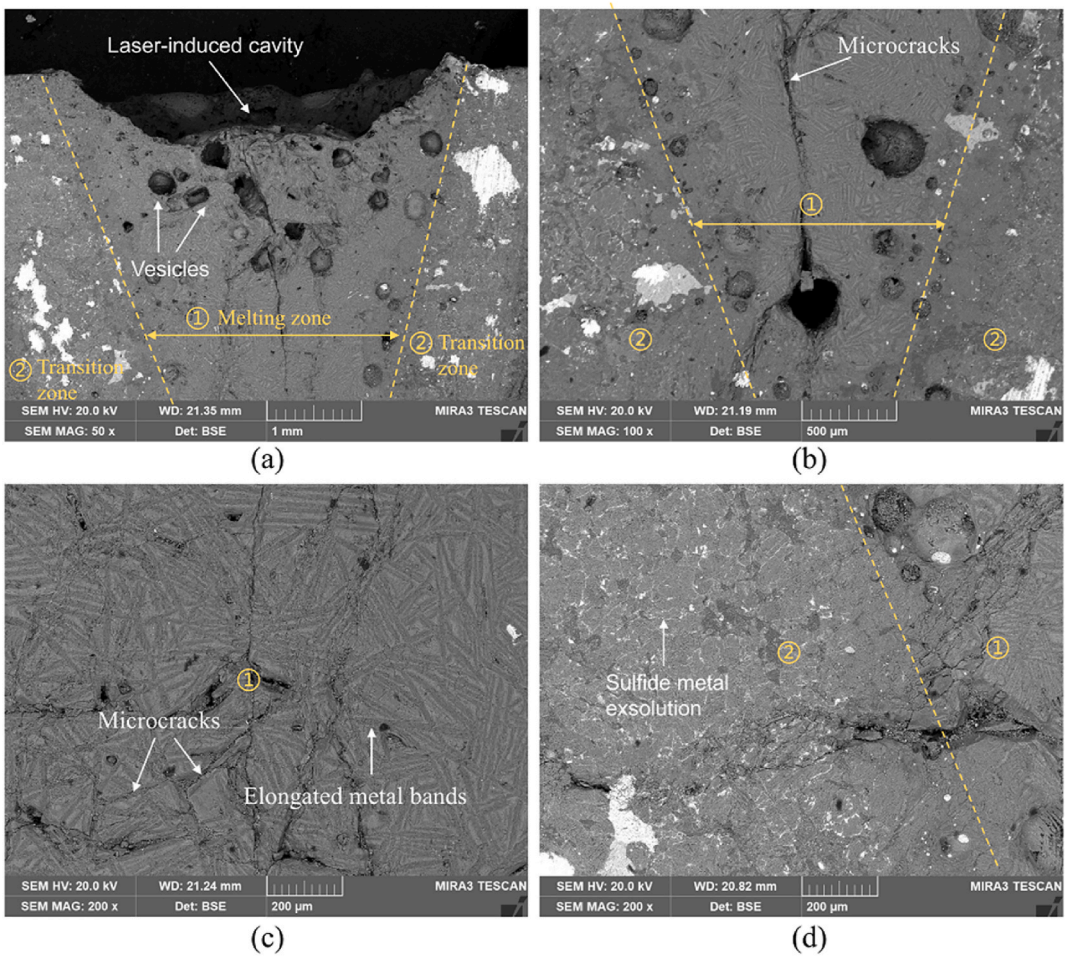


Fig. 10. Recrystallization of the mixture zone in the HaH 346 meteorite after cooling. (a) Internal profile of the laser-induced cavity. (b) Sulfide metal cavities were observed in the melt. (c) Elongated, needle-like crystal textures within the melt. (d) White mineral veins formed by sulfide metal exsolution.

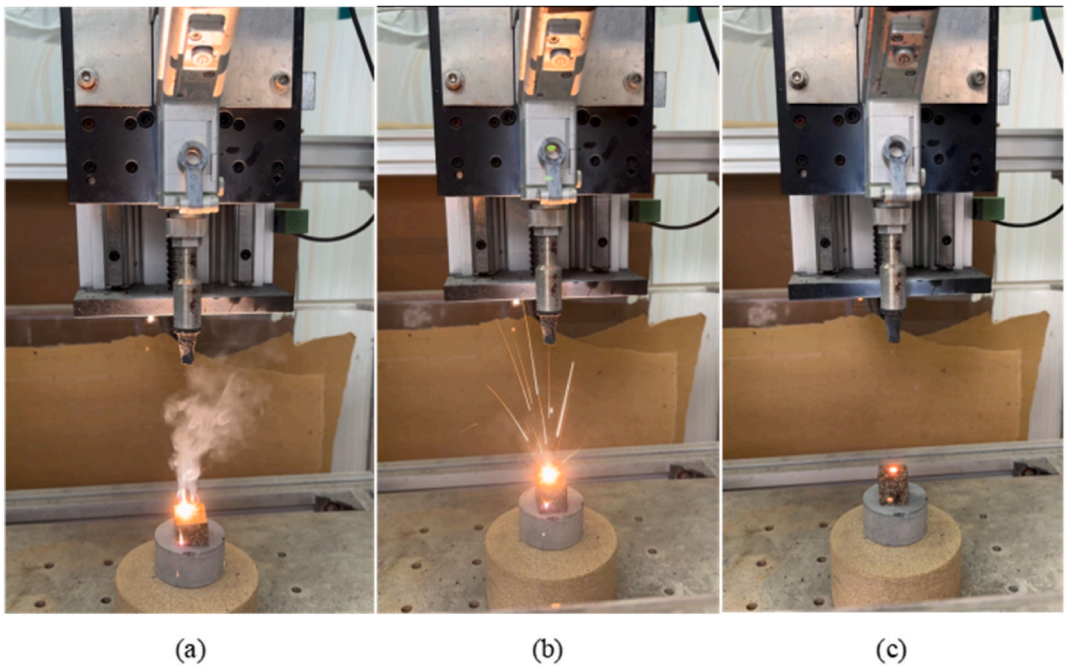


Fig. 11. (a) Smoke observed during laser ablation of silicates. (b) High-temperature fragments and molten material ejected due to laser-induced spallation and sputtering. (c) High-temperature molten pool of Fe-Ni metal immediately after laser removal.

changes and unique features—such as impact melt veins or high-pressure minerals—may form and influence their thermal behavior, warranting further investigation. Finally, this study used fixed laser parameters. Future work will explore how varying laser parameters affect the melting behavior and morphology of Fe-Ni metals.

8. Conclusions

The present study provides a comprehensive analysis of the effects of Fe-Ni metals on the laser-induced melting and cavity formation in chondrite meteorites. Through a series of laser irradiation experiments, we have demonstrated that the presence of Fe-Ni metals significantly influences the interaction between the laser and HaH 346 chondrite meteorite. The findings have direct implications for space mining on S-type asteroids and other planetary bodies with oxygen-deficient atmospheres, where rocks often contain iron-nickel or elemental iron. These insights help predict laser-rock interactions in extraterrestrial environments, supporting the development of laser-based mining technologies. The main conclusions drawn from this research are as follows:

(1) Fe-Ni metal content significantly affects the depth and morphology of laser-induced cavities. Zones with higher Fe-Ni metal content produce shallower and wider cavities due to the rapid absorption of laser energy and the shielding effect of metals.
(2) Fe-Ni metals reach significantly lower temperatures during laser irradiation compared to silicates. The maximum temperature in the Fe-Ni metal zone was 1034.4 °C, whereas the silicate zone reached 1710.7 °C. This difference arises from the high reflectivity and thermal conductivity of Fe-Ni metals, which limit energy absorption and temperature increase.
(3) Fe-Ni metals recrystallize into unique ellipsoidal crystal formations after cooling, while silicates form complex marble-like and nest-like structures. In the mixture zone, elongated needle-like metal crystals are observed, resulting from the immiscibility of Fe-Ni metal melt and silicate melts.

CRediT authorship contribution statement

Yiwei Liu: Writing – original draft, Investigation, Funding acquisition, Data curation. **Yanlong Zheng:** Writing – review & editing, Conceptualization. **Yi Hu:** Supervision, Resources. **Shimin Liu:** Writing – review & editing, Supervision. **Haizeng Pan:** Investigation. **Xuhai Tang:** Writing – review & editing, Funding acquisition.

Declaration of competing interest

☑ The authors declare that they have no known competing financial interests or personal relationships that could have appeared to influence the work reported in this paper.

Acknowledgments

This work was jointly supported by National Natural Science Foundation of China (Grants No. 42402285, 12172264, and 52174004), the Postdoctoral Fellowship Program (Grade B) of China Postdoctoral Science Foundation (Grant No. GZB20230544), and Shenzhen Science and Technology Program (Grant No. JCYJ20230807090102006).

References

1. Andrews DG, Bonner KD, Butterworth AW, et al. Defining a successful commercial asteroid mining program. *Acta Astronaut.* 2015;108:106–118.
2. Campbell JW. *Using Lasers in Space - Laser Orbital Debris Removal and Asteroid Deflection*. vol. 20. 2000.
3. Lietaert K, Thijs L, Neirinck B, et al. Meteorite as raw material for Direct Metal Printing: a proof of concept study. *Acta Astronaut.* 2018;143(July 2017):76–81. https://doi.org/10.1016/j.actaastro.2017.11.027.
4. Vetrisano M, Colombo C, Vasile M. Asteroid rotation and orbit control via laser ablation. *Adv Space Res.* 2016;57(8):1762–1782. https://doi.org/10.1016/j.asr.2015.06.035.
5. Song YJ, Park SY. Estimation of necessary laser power to deflect near-Earth asteroid using conceptual variable-laser-power ablation. *Aero Sci Technol.* 2015;43:165–175. https://doi.org/10.1016/j.ast.2015.02.022.
6. Anthony N, Frostevarg J, Suhonen H, Granvik M. Laboratory experiments with a laser-based attachment mechanism for spacecraft at small bodies. *Acta Astronaut.* 2021;189(March):391–397. https://doi.org/10.1016/j.actaastro.2021.08.028.
7. Anthony N, Frostevarg J, Suhonen H, Wanhainen C, Penttilä A, Granvik M. Laser processing of minerals common on asteroids. *Opt Laser Technol.* 2021;135(November 2020). https://doi.org/10.1016/j.optlastec.2020.106724.
8. Hellgren V. Asteroid mining: a review of methods and aspects. *Student thesis Ser INES*. 2016. Published online.
9. Hein AM, Saidani M, Tollu H. Exploring potential environmental benefits of asteroid mining. *arXiv Prepr arXiv181004749*. 2018. Published online.
10. Zacny K, Cohen MM, James WW, Hilscher B. Asteroid mining. In: *AIAA Space 2013 Conference and Exposition*. 2013:5304.
11. Fateri M, Gebhardt A. Process parameters development of selective Laser Melting of lunar regolith for on-site manufacturing applications. *Int J Appl Ceram Technol.* 2015;12(1):46–52. https://doi.org/10.1111/ijac.12326.
12. Neumann J, Ernst M, Taschner P, et al. The MOONRISE: payload for mobile selective laser melting of lunar regolith. *Int Conf Space Optics—ICSO 2020*. 2021;11852:2791–2798.
13. Zhou C, Chen R, Xu J, et al. In-situ construction method for lunar habitation: Chinese Super Mason. *Autom ConStruct.* 2019;104(March):66–79. https://doi.org/10.1016/j.autcon.2019.03.024.
14. Zhou C, Gao Y, Zhou Y, et al. Properties and characteristics of regolith-based materials for extraterrestrial construction. *Engineering.* 2024;37:159–181. https://doi.org/10.1016/j.eng.2023.11.019.
15. Dreyer Christopher B, Sercel Joel, Gertsch Leslie, Alex Lampe TJC, AAM. *Optical mining subscale testing. Earth Sp*. 2016:493–506. Published online.
16. Anthony N, Frostevarg J, Suhonen H, Wanhainen C, Granvik M. Laser-induced spallation of minerals common on asteroids. *Acta Astronaut.* 2021;182(February):325–331. https://doi.org/10.1016/j.actaastro.2021.02.018.
17. Matsuoka M, Nakamura T, Kimura Y, et al. Pulse-laser irradiation experiments of Murchison CM2 chondrite for reproducing space weathering on C-type asteroids. *Icarus.* 2015;254:135–143. https://doi.org/10.1016/j.icarus.2015.02.029.
18. Hamann C, Luther R, Ebert M, et al. Correlating laser-generated melts with impact-generated melts: an integrated thermodynamic-petrologic approach. *Geophys Res Lett.* 2016;43(10):10602–10610. https://doi.org/10.1002/2016GL071050. Received.
19. Tang X, Xu J, Zhang Y, et al. The rock-forming minerals and macroscale mechanical properties of asteroid rocks. *Eng Geol.* 2023;321(May), 107154. https://doi.org/10.1016/j.enggeo.2023.107154.
20. Christensen NI. Poisson's ratio and crustal seismology. *J Geophys Res Solid Earth.* 1996;101(2):3139–3156. https://doi.org/10.1029/95jb03446.
21. Barthelmy D. https://webmineral.com.
22. Srinivas M, Malakondaiah G, Rao PR. Fracture toughness of f.c.c. nickel and strain ageing b.c.c. iron in the temperature range 77-773 K. *Acta Metall Mater.* 1993;41(4):1301–1312. https://doi.org/10.1016/0956-7151(93)90181-Q.
23. Koizumi S, Hiraga T, Suzuki TS. Vickers indentation tests on olivine: size effects. *Phys Chem Miner.* 2020;47(2):8.
24. Scheidl KS, Schaeffer AK, Petrishcheva E, et al. Chemically induced fracturing in alkali feldspar. *Phys Chem Miner.* 2014;41:1–16.
25. Xu J, Zhang Y, Rutqvist J, Hu M, Wang Z, Tang X. Thermally induced microcracks in granite and their effect on the macroscale mechanical behavior. *J Geophys Res Solid Earth.* 2023;128(1). https://doi.org/10.1029/2022JB024920.
26. Tang C, Li S. The Earth evolution as a thermal system. *Geol J.* 2016;51(S1):652–668. https://doi.org/10.1002/gj.
27. Tang C, Chen T, Gong B. Earth's thermal cycles and major geological events. *Sci China Earth Sci.* 2021;64(10):1821–1824. https://doi.org/10.1007/s11430-021-9805-0.